On the Use of the Geometric Median in Delay-and-Sum Ultrasonic Array Imaging

Nicolas Budyn

Abstract—**Delay-and-sum algorithms are imaging techniques in nondestructive testing, which form images by summing backpropagated signals. Under this approach, a small number of high-intensity signals, such as those from boundary reflections, may create artifacts that degrade the image and hinder defect detection. This article introduces a probabilistic model of the summation, which explains the origin of this effect and proposes to replace the summation in the imaging algorithm by the more statistically robust geometric median. As demonstrated on an experimental inspection using multiview total focusing method and plane wave imaging, this novel technique effectively suppresses some artifacts, at the expense of an increase in the structural noise amplitude and additional diffraction artifacts at the ends of some structural features. As such, the geometric median provides an alternative imaging approach that may improve the performance in some circumstances.**

Index Terms—**Array signal processing, phased arrays, ultrasonic imaging.**

I. INTRODUCTION

IN ULTRASONIC nondestructive testing, delay-and-sum imaging algorithms are a class of established techniques that form an image by synthetically backpropagating the ultrasonic wave field as a postprocessing step, which leads to a constructive interference of the target signal and a destructive interference of the noise [1]. This is known in medical ultrasound as synthetic aperture imaging [2]. Several approaches exist; they generally use the same delay laws in reception but differ in how the specimen is insonified. The total focusing method (TFM) emulates a wave converging at the image point by postprocessing the data from all combinations of transmitters and receivers, known as the full matrix capture (FMC) [3], [4]. The synthetic aperture focusing technique (SAFT) is similar to TFM except that it only exploits signals where the transmitter coincides with the receiver [5]. The plane wave imaging (PWI) algorithm uses plane waves [6]. The virtual source aperture technique uses spherical waves diverging from a point behind or in front of the array [7], [8].

Multiple images of the same specimen can be formed with any of these techniques by exploiting different wave modes including or not a reflection against the back wall, an approach known as multimode or multiview imaging. As the recorded

ultrasonic data contain a superposition of wave modes, imaging with one mode leads to the creation of artifacts in the image caused by the others [9]. Existing artifact filtering techniques are based on the identification (manually or with a threshold) and then suppression (with zeroing or subtraction) of the signal that creates artifacts in other views [9], [10]. Another artifact filtering strategy consists in reducing the influence of unphysical ultrasonic paths in the reconstruction using appropriate weights, which has been done in composite materials [11] and for planar defects [10]. The weights may also be chosen based on the signal statistics, an approach termed adaptive beamforming [12]–[14]. A different strategy to mitigate the influence of artifacts, when a specific defect type can be assumed, is to only consider views where the known defect has a significant amplitude [15], [16].

In all delay-and-sum techniques, the pixel amplitude is obtained by summing ultrasonic signals to achieve constructive interference of the defect signal and destructive interference of the noise. Using probabilistic modeling, this article demonstrates that the summation is justified for normally distributed noise but may cause imaging artifacts in case of contamination by high amplitude spurious signals, such as boundary reflections. This article replaces the summation by the more statistically robust geometric median to achieve the suppression of some artifacts. The consequences for the defect signal-to-noise ratio (SNR), the noise, and the artifacts are explored, and the experimental results are presented for the inspection of a copper block using TFM and PWI.

II. DELAY-AND-SUM ALGORITHMS IN ULTRASONIC ARRAY IMAGING

Consider an ultrasonic array of N elements. The continuous-time signal transmitted by element i and recorded by element j is denoted $f_{ij}(t)$; it can be obtained from its discrete-time equivalent with any interpolation technique; the Lanczos interpolation [17] is used here. The full matrix capture (FMC) data are the set of the N^2 time signals $\{f_{ij}(t) : i = 1..N, j = 1..N\}$. An image can be formed by postprocessing the FMC using the TFM [3], [4]

$$I_0^{\text{TFM}}(\mathbf{r}) = \sum_{i=1}^{N} \sum_{j=1}^{N} \tilde{f}_{ij}(\tau_{ij}(\mathbf{r})) \qquad (1)$$

where $\left|I_0^{\text{TFM}}(\mathbf{r})\right|$ is the pixel amplitude at position $\mathbf{r}$, $\tilde{f}_{ij}(t)$ is the analytic (complex) signal obtained with the Hilbert transform, and $\tau_{ij}(\mathbf{r})$ is the propagation time corresponding to the ray path from the transmitter i to the position $\mathbf{r}$ and finally
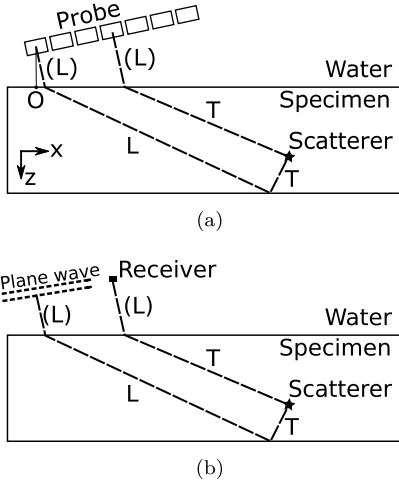
Fig. 1.   Inspection configuration. The rays shown correspond to (a) TFM view LT–T and (b) PWI view LT–T, where L stands for longitudinal and T for transverse. The point O is the origin of the coordinate system.

to the receiver j, calculated with any suitable ray-tracing technique. Apodization is ignored here but could be included if desired. Different images, or views, are obtained by considering ray paths that include or not a reflection against the back wall and are either longitudinal (L) or transverse (T) waves; for example, Fig. 1(a) shows the TFM view LT–T, where LT is the ray path from the transmitter to the scatterer and T is the path from the scatterer to the receiver; this nomenclature ignores the ray leg in the water, which is always longitudinal. In (1), first, the double sum is rewritten as a single sum, second, the notation $x_k := \tilde{f}_{ij}(\tau_{ij}(\mathbf{r}))$ is used for brevity, and third, the result is scaled by $n := N^2$, leading to

$$I_1^{\mathrm{TFM}}(\mathbf{r}) = \frac{1}{n} \sum_{k=1}^{n} x_k \qquad (2)$$

where $I_0^{\mathrm{TFM}}(\mathbf{r})$ and $I_1^{\mathrm{TFM}}(\mathbf{r})$ are equal up to a multiplicative factor $1/n$; as an image is generally rescaled by an arbitrary image point, this factor has no practical consequence. However, it becomes clear with (2) that $I_1^{\mathrm{TFM}}(\mathbf{r})$ is the (complex) mean of $\{x_k : k = 1..n\}$.

A PWI algorithm [6] has a similar form

$$I_0^{\mathrm{PWI}}(\mathbf{r}) = \sum_{q=1}^{Q} \sum_{j=1}^{N} \tilde{g}_{qj}(\tau_{qj}(\mathbf{r})) \qquad (3)$$

where $g_{qj}(t)$ is the time signal corresponding to the qth emitted plane wave and the jth receiver and $\tau_{qj}(\mathbf{r})$ is the total propagation time of the qth plane wave from the probe to the image point and a cylindrical wave from the image point to the receiver j. As for the TFM algorithm, several views can be formed; for example, Fig. 1(b) shows the PWI view LT–T, where LT is the plane wave path in transmission and T is the cylindrical wave path in reception. Again, this equation can be rewritten (up to a scaling n) as

$$I_1^{\mathrm{PWI}}(\mathbf{r}) = \frac{1}{n} \sum_{k=1}^{n} x_k \qquad (4)$$

with this time $x_k := \tilde{g}_{qj}(\tau_{qj}(\mathbf{r}))$ and $n := N \times Q$.

In conclusion, delay-and-sum algorithms form an image pixel by taking the mean of appropriately chosen data points. The consequence of this operation is explored in the following sections.

III. PROBABILISTIC MODELING OF NOISE AND SIGNAL

A. Theory

A probabilistic model of the ultrasonic data x_k in the absence or presence of a defect is introduced in this section. Following Wilcox [1], two sources of noise are considered: the random noise (thermal acoustic noise in the sample and electronic noise in the instrumentation), and the coherent noise, which includes grain noise. The random noise can be suppressed by averaging multiple independent transmissions but the coherent noise cannot, which ultimately limits the defect detectability. The grain noise is caused by the interaction of the elastic wave with the material microstructure. It is classically modeled as the superposition of grain scattering events [18], [19]. Each grain response is assumed to have the same amplitude and a uniformly distributed phase. Ignoring multiple scattering, the grain responses are independent, and by the central limit theorem, their superposition is the spherically symmetric normal distribution

$$x_k^{\mathrm{grain}} \sim \mathrm{Normal}(0, \sigma^2 \mathbf{1}). \qquad (5)$$

The complex random variable x_k is interpreted for clarity as a 2×1 real random vector $\begin{bmatrix} \mathrm{Re}(x_k) & \mathrm{Im}(x_k) \end{bmatrix}^T$. Normal stands here for the bivariate normal distribution; its mean is the 2×1 vector $\begin{bmatrix} 0 & 0 \end{bmatrix}^T$, also denoted 0, and its 2×2 covariance matrix is the product of the 2×2 identity matrix $\mathbf{1}$ by the (scalar) variance σ^2. In a first approximation, $\{x_k\}_k$ are assumed to be independent, so their mean is also normally distributed

$$I_1^{\mathrm{grain}}(\mathbf{r}) = \frac{1}{n} \sum_{k=1}^{n} x_k^{\mathrm{grain}} \sim \mathrm{Normal}\left(0, \frac{1}{n}\sigma^2 \mathbf{1}\right) \qquad (6)$$

where $I_1(\mathbf{r})$ is I_1^{TFM}, I_1^{PWI}, or another delay-and-sum algorithm. As a consequence, $\left| I_1^{\mathrm{grain}}(\mathbf{r}) \right|$ is Rayleigh distributed, which was experimentally validated on B-scans [18] and TFM images [20].

The signal in the presence of a defect is modeled as the addition of the deterministic defect response, μ, and the grain noise

$$x_k^{\mathrm{defect}} = \mu + x_k^{\mathrm{grain}} \qquad (7)$$

which leads to

$$x_k^{\mathrm{defect}} \sim \mathrm{Normal}(\mu, \sigma^2 \mathbf{1}) \qquad (8)$$

and

$$I_1^{\mathrm{defect}}(\mathbf{r}) = \frac{1}{n} \sum_{k=1}^{n} x_k^{\mathrm{defect}} \sim \mathrm{Normal}\left(\mu, \frac{1}{n}\sigma^2 \mathbf{1}\right). \qquad (9)$$

Note that the variation of the defect response with respect to the angles of the incident and scattered waves and the variation of transmission and reflection coefficients at the interfaces are neglected, which is reasonable for a narrow insonification beam typical in the multiview immersion
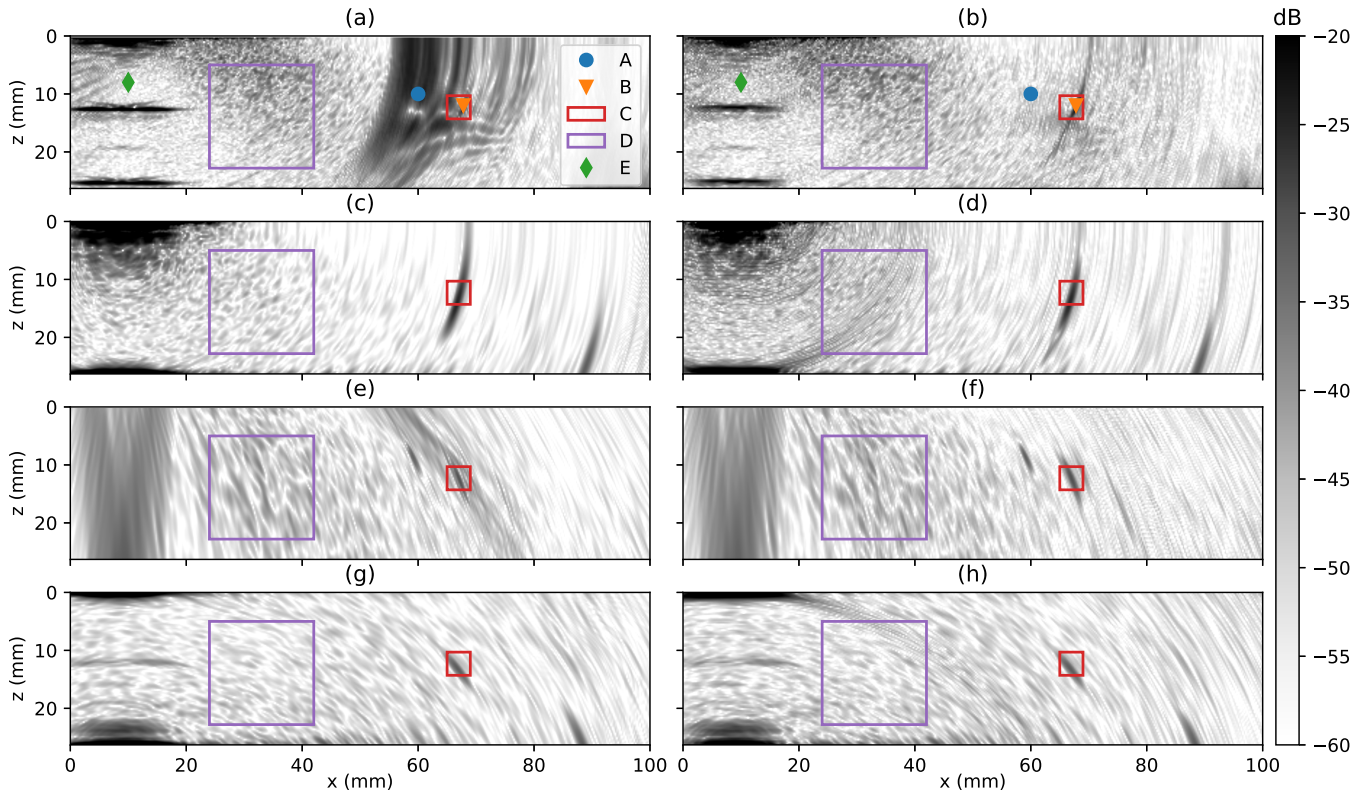
Fig. 2. Comparison of TFM images using (a), (c), (e), and (g) mean and (b), (d), (f), and (h) median. Rows from top to bottom: T–T, L–L, LT–T, and LL–LL. Common dB scale, where 0 dB is the peak amplitude of the back wall in (c). An artifact created by the front wall reflection is visible in (a) around point A. Square C surrounding the defect is used for SNR measurement. Square D is used for speckle level comparison.

inspections studied here. Physically, summing x_k creates a constructive interference of the defect response and a destructive interference of the noise. Note that estimating the parameter μ from $\{x_k\}$ is known in statistics as the location problem; the mean of x_k is an example of a location estimator. This last equation shows that the image point has a $\sqrt{n}$-times higher SNR than the time signals. This must be seen as a theoretical upper limit; in practice, the SNR increase is smaller because the time signals are correlated because the probe elements are spatially close to each other, so $\{x_k\}$ are not truly independent, and the variation of defect response may not be negligible ($\mu \neq \mu_k$). Nevertheless, this model illustrates how averaging signals through delay-and-sum imaging improves the SNR up to a certain point. A more important limit, in which this article aims to address, is that there are other sources of coherent noise than grain noise; other ultrasonic signals have arrival times that may coincide with the delay laws used to image a point, for example, boundary reflections, whose amplitudes may be an order-of-magnitude higher than the defect response or the grain noise. These spurious signals contaminate only a fraction of $\{x_k\}$, as their physical source is not located at the image point $\mathbf{r}$ for which the delay laws are tuned; however, they may have a detrimental effect as illustrated next with experimental data.

B. Experimental Validation and Discussion

Consider the inspection configuration presented in Fig. 1. The 64-element 5-MHz ultrasonic linear array (pitch 0.3 mm)

is held above the top surface with an angle of 12°. The distance between the closest probe element and the top surface is 30 mm. The specimen is a 26.3-mm-thick copper block (longitudinal velocity $v_L = 4730$ m/s and shear velocity $v_T = 2280$ m/s) with a side-drilled hole (SDH) of 2 mm diameter centered at $x = 67$ mm and $z = 12.5$ mm. Fig. 2(a), (c), (e), and (g) presents multiple TFM images of the sample: the SDH located at point B is clearly identified in the views L–L, LT–T, and LL-LL, but the artifact located near point A in the view T–T [see Fig. 2(a)] hinders the detection. This artifact corresponds to the second front wall reflection whose arrival time coincidences partially with the delay laws used in this view. Moving the probe further away from the sample would shift it or make it disappear; however, this solution may not be practical due to limited accessibility. In an inspection using a solid wedge rather than liquid couplant, similar echoes would be created by reflections in the wedge.

Before studying this artifact, point E is first considered. Point E is virtually pure grain noise as all signals except the front wall echo have greater times of flight. Fig. 3 shows the ultrasonic data points x_k that contribute to this pixel. The points are scattered in all directions and are approximately centered on zero; their density decreases with the distance to zero. As shown in Fig. 3(b), the normal distribution, fitted with the sample mean and the sample standard deviation, fits the data very well. Therefore, the grain noise model (5) appears to accurately explain the observed data. As a consequence, the resulting TFM amplitude, modeled by (6), is close to zero, as desired for grain noise.
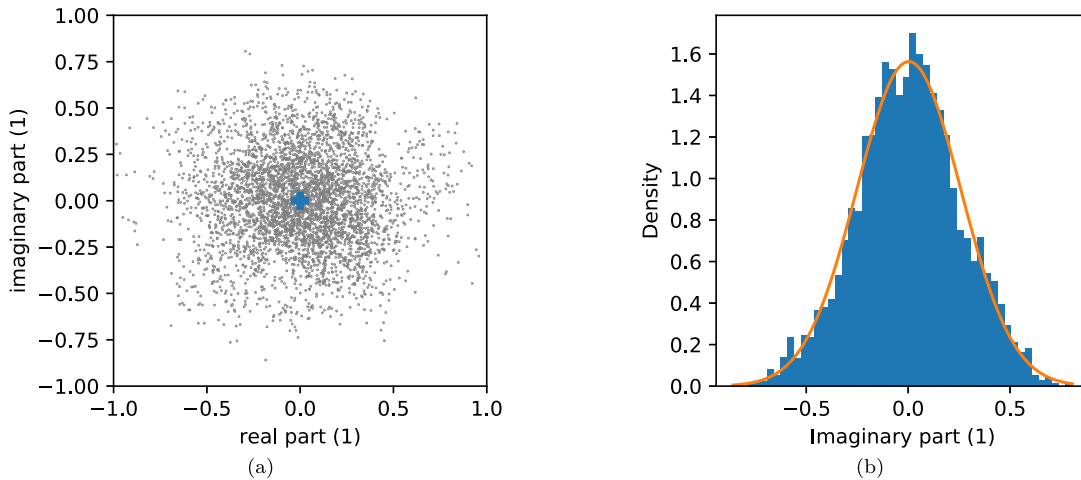
Fig. 3. Ultrasonic data $\{x_k\}$ that contribute to point E (grain noise) in TFM view T–T. (a) Scatter plot, full range. The blue cross indicates the (0, 0) point. (b) Histogram of the imaginary part and fit normal distribution.

The ultrasonic data contributing to the artifact are more pathological. Fig. 4 shows the points that form pixel A, and their empirical density obtained with kernel density estimation [21]. As for point E, there is a cluster of points spherically distributed around zero in a 0.25 radius, which corresponds to the grain noise. However, there is a halo of points of magnitude up to 16.6 which is left unexplained by the normal distribution; the probability of having points further away than a few standard deviations from the mean is practically zero due to the exponential decay of the density function. This halo is actually caused by the reflection of the front wall of the sample, not by the grain noise. If an image was formed with only the point in the main cluster (magnitude less than 0.25, 78% of the points), the TFM amplitude at this pixel would be 0.0028 (−51 dB), i.e., the grain noise floor; however, including all points leads to an amplitude of 0.055 (−25 dB), which demonstrates the strong influence of the 22% remaining points. As shown in Fig. 4(c), the mean point differs significantly from zero, which ultimately causes the artifact in and near pixel A.

The ultrasonic data points contributing to the defect image (point B) are shown in Fig. 5. Compared with pixel E, the cloud of points is shifted away from zero, due to the presence of the defect, which is consistent with the signal model introduced earlier [see (8)]. The points have a higher dispersion than for pixel E, likely because the defect response itself is dispersed; this is neglected in the model (8) and has little practical importance here. There are also high magnitude points, unexplained by the normal distribution, which may correspond to boundary echoes; contrary to point A, they have little effect here as they are not coherent.

This brief analysis shows that the normal distributions [see (5) and (8)] are appropriate to model the bulk of the data but not the remaining large spurious signals. A proper probabilistic treatment of them is difficult, yet they cannot be ignored as they may significantly degrade the image. The solution explored in this article is to aim to mitigate their influence using robust statistics.

IV. ROBUSTNESS/EFFICIENCY TRADEOFF

This section presents the fundamental results of robust statistics in the univariate case for simplicity, following Tukey [22], Huber [23], and Yohai [24, Ch. 2]. The objective is to obtain an estimate of μ from n measurements $x_k = \mu + \varepsilon_k$, where ε_k is a zero-centered noise. For normally distributed noise $\varepsilon_k \sim \text{Normal}(0, \sigma^2)$, the sample mean $\sum_{k=1}^{n} x_k/n \sim \text{Normal}(\mu, \sigma^2/n)$ is the optimal estimator in the sense that it has the lowest possible asymptotic (i.e., for large n) variance. However, real data are not always that well-behaved; one can consider instead Tukey's contaminated normal distribution, which models the presence of 5% of outliers of higher variance

$$x_k \sim 0.95\,\text{Normal}(\mu, \sigma^2)) + 0.05\,\text{Normal}(\mu, 100\sigma^2)). \quad (10)$$

The mean of n samples of this distribution is Normal $(\mu, 5.95\sigma^2/n)$. The presence of outliers causes a large increase of the variance of the mean, in which statisticians refer to as the lack of robustness of the mean. This detrimental effect becomes even higher when the proportion of outliers or their variance increase. The fundamental reason is that the mean minimizes $\sum_{k=1}^{n}(x_k - \hat{\mu})^2$, which gives a great influence to large $|x_k - \hat{\mu}|$ due to the square.

An alternative to the mean is the median, which is the value separating the higher half from the lower half of the data. Another characterization is that the median minimizes $\sum_{k=1}^{n} |x_k - \hat{\mu}|$; there is no square in contrast to the mean. The median of n samples is, for large n, Normal$(\mu, 1.57\sigma^2/n)$ for the normal distribution and Normal$(\mu, 1.72\sigma^2/n)$ for the contaminated normal distribution above; the presence of outliers causes only a mild increase (10%) of the variance of the median, which is why it is described as being more robust than the mean. The main drawback is that in the absence of outliers (x_k normally distributed), the median has a 57% higher variance than the mean, in which statisticians refer to as a lower efficiency at the normal distribution. Choosing the mean or the median is essentially a robustness/efficiency tradeoff. Although the contaminated normal may not be an accurate
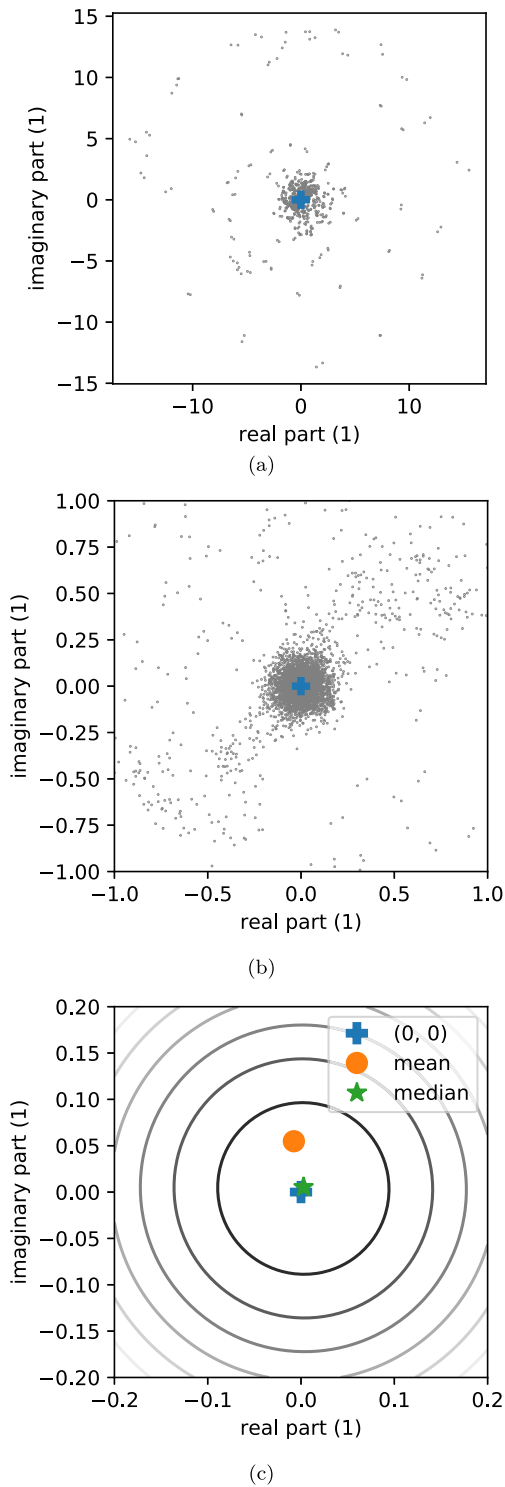
Fig. 4. Ultrasonic data $\{x_k\}$ that contribute to point A (artifact) in TFM view T–T. (a) Scatter plot, full range. (b) Scatter plot, clipped. (c) Contour of the empirical density function, clipped.

Fig. 5. Ultrasonic data $\{x_k\}$ that contribute to point B (defect) in TFM view T–T. (a) Scatter plot, full range. (b) Scatter plot, clipped. (c) Contour of the empirical density function, clipped.

model for ultrasonic data, it illustrates how a robust statistic can mitigate the detrimental effect of a limited number of high amplitude signals.

V. GEOMETRIC MEDIAN

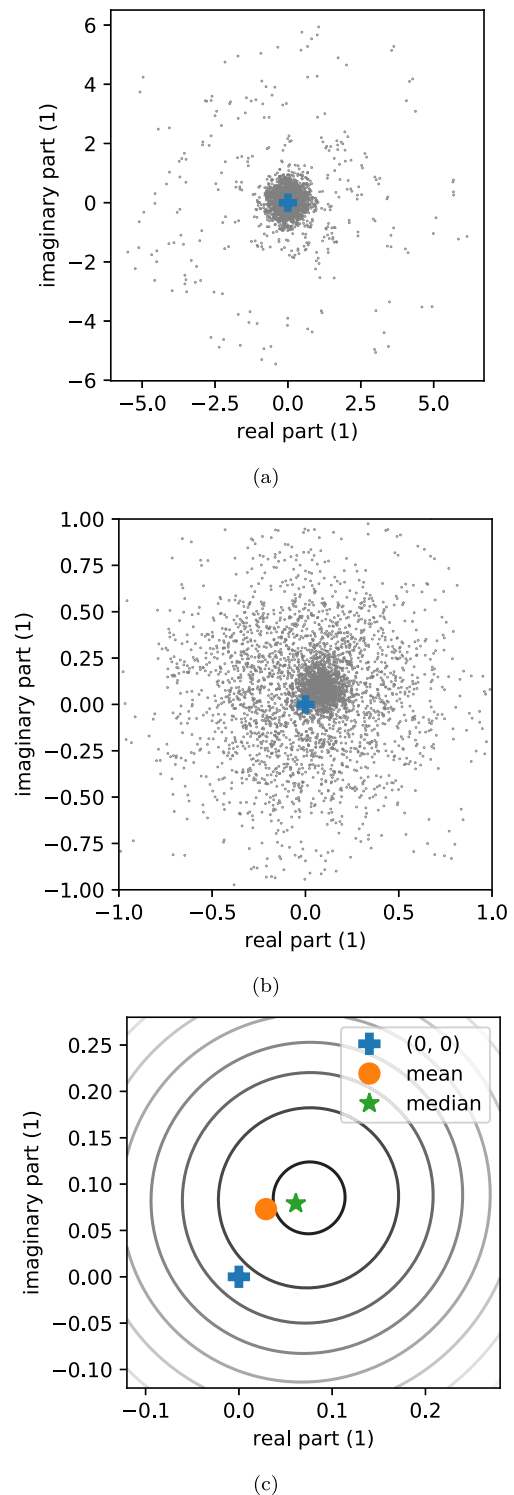As seen previously, the delay-and-sum algorithm is essentially the mean of complex data, or equivalently, 2-D real

vectors. Also, the mean lacks robustness, which makes it a suboptimal estimator in the presence of outliers; this was presented in the previous section in the univariate case but remains true in the bivariate case [25, Ch. 6]. Therefore, one may wish to replace the mean in the delay-and-sum algorithm by a more robust estimator. Massé and Plante compared ten bivariate location estimators with a Monte Carlo study

using 26 different noise distributions and concluded that the geometric median "clearly stands as the best overall" [26]. The geometric median, also known as the spatial median, L_1 median or L_1 estimator, is defined as the point minimizing the Euclidean distance to all data points, that is [27]

$$\text{Median}\{x_k\} = \arg\min_{x \in \mathbb{R}^2} \sum_{k=1}^{n} \|x_k - x\|_2. \tag{11}$$

This extends the univariate median to multiple dimensions as the 1-D median minimizes the sum of absolute values to all data points [$|\cdot|$ instead of $\|\cdot\|_2$ in (11)]. Taking the gradient of the sum of distances leads to a second equivalent definition; the geometric median is the solution of $S(x) = 0$ with

$$S(x) = \sum_{k=1}^{n} \frac{x - x_k}{\|x - x_k\|_2}. \tag{12}$$

This calls for three remarks, borrowed from the thorough theoretical analysis made by Hettmansperger and McKean [25, Ch. 6]. First, $S(x)$ is a sum of unit vectors, so the geometric median depends on the direction of the vector $x - x_k$ rather than its magnitude, which explains why the magnitude of individual values has no influence. Second, the geometric median is more robust than the mean but has a lower efficiency for the spherically symmetric bivariate normal distribution (variance increased by 27%); as in the univariate case, efficiency and robustness are being traded. Third, the geometric median is different from the componentwise median, which is the vector of the univariate medians component by component; the geometric one is invariant by the rotation of the complex plane, whereas the componentwise one is not; the geometric median has also a higher efficiency than the componentwise one for spherical distributions (see also Small [28] for a survey of multidimensional medians).

As an alternative to the classic delay-and-sum imaging algorithm is introduced

$$I_2(\mathbf{r}) = \text{Median}\{x_k : k = 1..n\} \tag{13}$$

where x_k corresponds to either TFM (2) or PWI (4). The consequences of replacing the mean by the median in imaging are twofold. First, due to the increased robustness, the noise in the pixels strongly affected by a small number of high amplitude data points will decrease. Second, due to the decreased efficiency, the noise in the pixels nonaffected by outlying data points will increase.

The geometric median is calculated numerically as it has no general closed-form expression. Fritz et al. [29] compared several algorithms and concluded that a Newton-type algorithm with a line search provides "a stable, fast and reliable approach" [29]. Newton's descent with backtracking line search [30, Algorithm 3.1] and analytically calculated Hessian that was used in this article.

VI. RESULTS

Fig. 2 shows the TFM images using the mean and the median for the views T–T, L–L, LT–T, and LL-LL. For PWI, the ultrasonic data are derived from the FMC. Different plane wave angles are used depending on the view to ensure a good insonification of the specimen and, in particular, of the defect. Sixteen plane waves are used per view. For the direct views, the refracted angles of the plane waves are linearly sampled between 0° and 85° for the plane wave L (used in views L–X and L–XY) and 10° and 85° for T (used in views T–X and T–XY). For the skip paths, the reflected angles of the final leg are linearly sampled between 30° and 60° for LL, 30° and 85° for TL, 10° and 24° for LT, and 30° and 60° for TT. Fig. 6 shows the PWI images using the mean and the median for the views LL–T, L–L, LT–T, and LL-LL. Overall, the mean and the median aggregation give similar images; the main differences are highlighted in the following section.

A. Artifacts

In contrast to the classic (mean) TFM view T–T, median TFM is not contaminated by the front wall artifact [see Fig. 2(a) and (b)]. The amplitude at point A is reduced by 20 dB, reaching the grain noise floor. This can be visualized in Fig. 4; the median is closer to 0 than the mean because it is less influenced by the outliers. The suppression of this artifact allows the area underneath to be correctly imaged and makes the scatterer B clearly visible. The same effect is observed to a lesser extent in TFM view LT–T [see Fig. 2(e) and (f)]. The median does not remove all artifacts; for example, the artifact at $(x = 60, z = 10)$ in the same view, which corresponds to the defect response for the wave mode LL–T, is left untouched because it is caused by a large number of coherent signals.

A drawback of median TFM is the smearing of the back wall as in view L-L [see Fig. 2(d)] or front wall as in LL-LL [see Fig. 2(h)]. The reason why these artifacts appear in the median image but not the mean one is not understood at this stage.

B. Noise Level

This section compares the noise root mean square (rms) in the 18×18 mm square D shown in Figs. 2 and 6 for all direct, half-skip, and full-skip views in TFM and PWI. This area was chosen to contain mainly speckle noise in TFM views. Redundant TFM views (example: L–T and T–L) were ignored. This leads to 21 TFM views and 36 PWI views.

The noise rms is increased by median TFM across all views by 1.6 dB ± 1.3 dB (mean ± standard deviation). The largest increase is 5.5 dB for the view L–L, caused mainly by the diffraction artifact near the back wall mentioned in the previous section. The overall increase of the speckle noise is consistent with the theoretical loss of efficiency of the median compared with the mean discussed in Sections IV and V; in the absence of spurious signals that create artifacts, the mean leads to a smaller noise level.

In PWI, the noise level seems dominated by numerous artifacts rather than the speckle, due to the limited number of transmissions. This is a situation where the median is advantageous (increased robustness): the noise rms in square D is reduced across all views by 0.2 dB ± 1.8 dB (mean ± standard deviation), maximum decrease: 6.2 dB, and maximum increase: 1.5 dB. The images produced by the median are also noticeably cleaner as artifacts are suppressed,
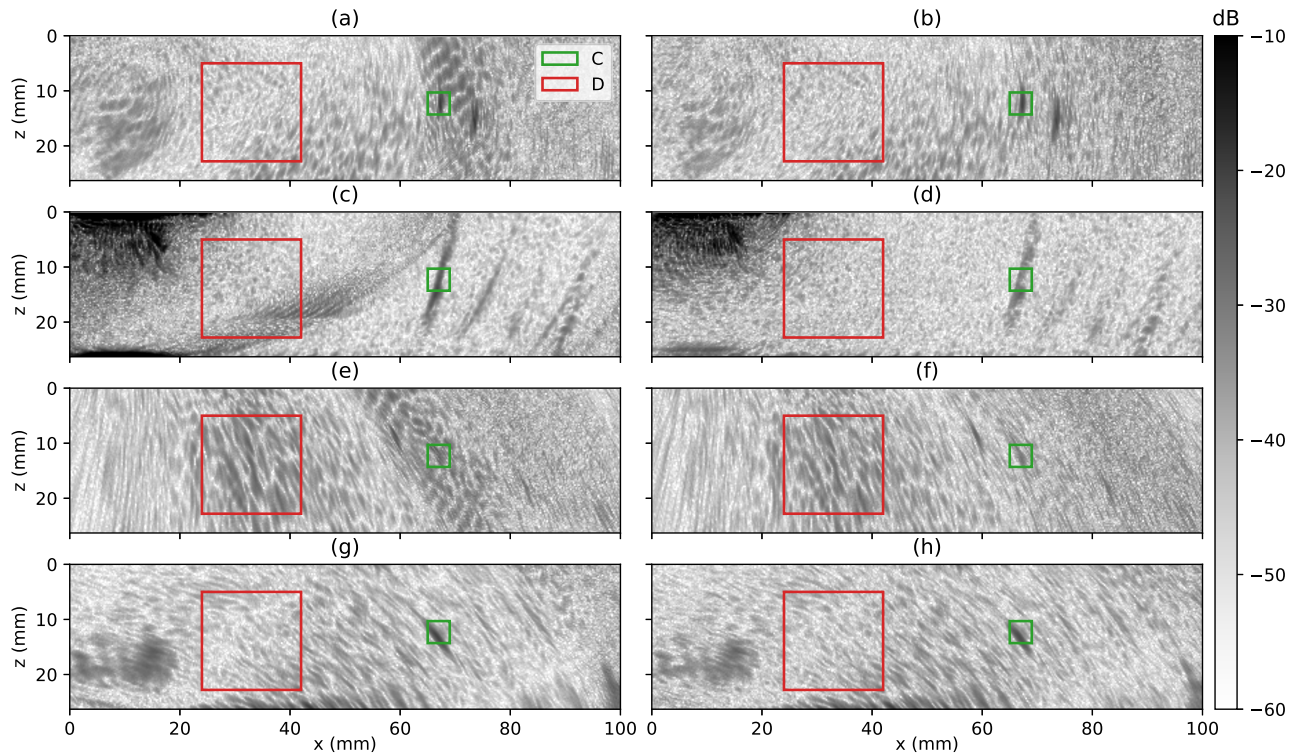
Fig. 6. Comparison of PWI images using (a), (c), (e), and (g) mean and (b), (d), (f), and (h) median. Rows from top to bottom: LL-T, L–L, LT–T, and LL–LL. Common dB scale, where 0 dB is the peak amplitude of the back wall in (c). The orange square corresponds to the scatterer.
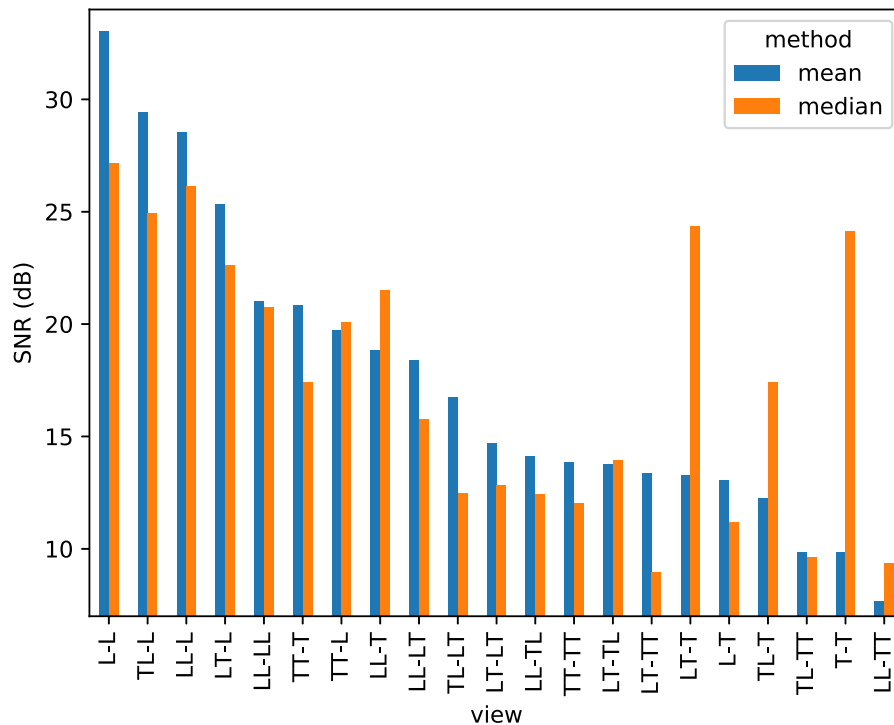

Fig. 7. SNR in TFM views measured in square C in Fig. 2. Higher is better.

C. Signal-to-Noise Ratio

The SNRs of the side-drilled hole were measured in the same views as in Section VI-B. The SNR is defined in this article as the ratio of the maximum image amplitude in the 4×4 mm square C surrounding the defect by the rms of pixels in the same area in a (not shown) defect-free acquisition. In the authors' opinion, the SNR threshold above which a signal clearly stands out from the noise is around 10 dB; however, it is not a clear cutoff. The SNR is used here as

for example, near the scatterer in views LL–T and LL-LL (first and third rows of Fig. 6).
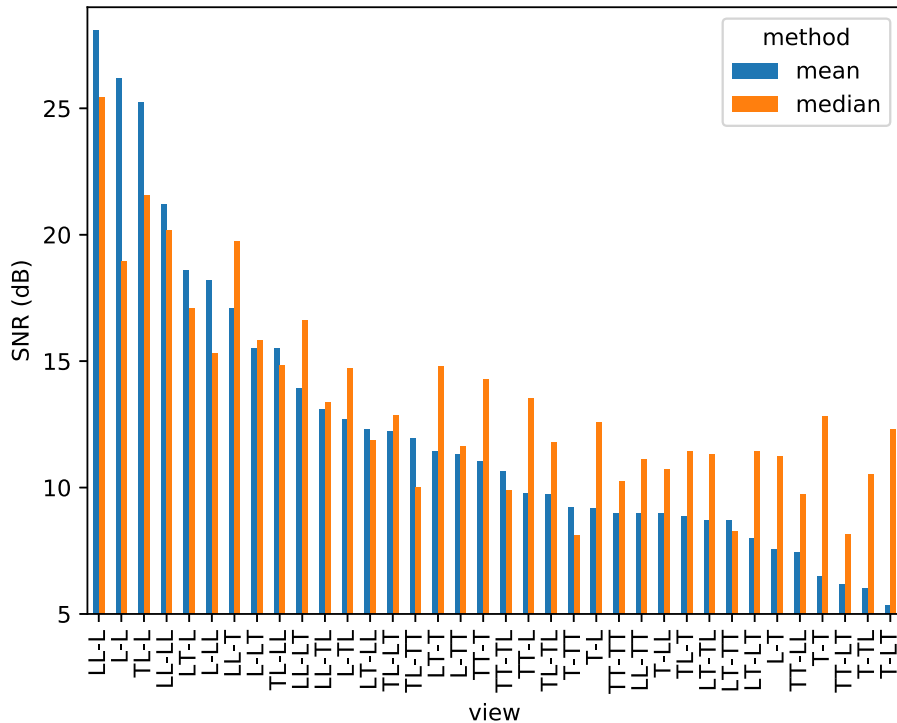
Fig. 8. SNR in PWI views measured in square C in Fig. 6. Higher is better.

a proxy for detectability, but it is not perfect; in practice, the presence of numerous echoes with high SNR may hinder the unambiguous identification of the defect; this scenario tends to happen for views with a relatively low SNR (under 15 dB).

Fig. 7 shows the SNR for each TFM view sorted by amplitude in the mean case. The signal amplitudes across all views are relatively constant (a difference of 0.8 dB $\pm$ 1.5 dB, mean $\pm$ standard deviation); the changes of SNR are mainly explained by a change of noise level. When the noise is dominated by the presence of artifacts, their suppression by the median leads to sharp increase of the SNR, as in T–T (14.3 dB) and LT–T (11.1 dB). When the noise is dominated by the speckle, the noise increases as seen previously, which ultimately decreases the SNR as in view L–L (-5.9 dB, largest degradation across all views). Overall, the average SNR is almost equal: 17.5 dB for the mean and 17.3 dB for the median.

Fig. 8 shows the SNR for each PWI view. The average SNR with the median (13.4 dB) is slightly better than with the mean (12.3 dB). The signal amplitudes with the median tend to be smaller (average difference of -1.3 dB), but the noise level is also lower (average difference of -2.4 dB) due to the suppression of artifacts. The largest SNR variations in both directions are at the view L–L [-7.2 dB, Fig. 6(c) and (d)] due mainly to a 5.7 dB decrease of the signal and at the view T–LT (7.0 dB) due to an artifact suppression.

VII. CONCLUSION

Delay-and-sum imaging techniques form images by averaging ultrasonic data. If the defect signal is polluted purely by grain noise that is accurately modeled as normally distributed additive noise, the mean is optimal for its suppression.

However, when accounting for other sources of unwanted image artifacts such as those caused by boundary reflections, the distribution of the polluting noise is only approximately normal; these high amplitude spurious signals have a large effect on the mean, which may ultimately lead to a degradation of the image. Replacing the mean by the more robust geometric median in the imaging algorithm allows the suppression of some artifacts and the recovery of signals underneath. The main drawbacks are the mild increase of the grain noise level due to the lower efficiency of the median for normally distributed data and additional diffraction artifacts at the ends of some wall echoes. The net effect on the SNR depends mainly on the noise mechanism; in the presence of an artifact, it is preferable to use the median, and in the presence of grain noise speckle, it is preferable to use the mean.

This novel imaging approach is philosophically different from the regular delay-and-sum approach as it is justified by a statistical model (the location problem) rather than physical considerations on constructive/destructive interference of waves. It is also nonlinear in the ultrasonic data. Contrary to existing artifact filtering methods, it is threshold-free and does not require any prior identification of problematic signals.

It would be interesting to combine both mean- and median-based images into a hybrid image that would retain the advantages of both approaches; it is yet unclear how to achieve this. Also, other than saying that the noise includes a small fraction of high amplitude outliers, a more precise model for the noise has intentionally not been introduced. For this reason, it is unknown whether the geometric median is the optimal location estimator to recover the scatterer signal. Finally, the use of the median in adaptive imaging could be assessed. These questions could be the subject of future work.

REFERENCES

[1] P. D. Wilcox, "Ultrasonic arrays in NDE: Beyond the B-scan," *AIP Conf. Proc.*, vol. 1511, pp. 33–50, Jan. 2013. [Online]. Available: http://scitation.aip.org/content/aip/proceeding/aipcp/10.1063/1.4789029

[2] J. A. Jensen, S. I. Nikolov, K. L. Gammelmark, and M. H. Pedersen, "Synthetic aperture ultrasound imaging," *Ultrasonics*, vol. 44, pp. e5–e15, Dec. 2006. [Online]. Available: http://www.sciencedirect.com/science/article/pii/S0041624X06003374

[3] C. Holmes, B. W. Drinkwater, and P. D. Wilcox, "Post-processing of the full matrix of ultrasonic transmit–receive array data for nondestructive evaluation," *NDT E Int.*, vol. 38, no. 8, pp. 701–711, Dec. 2005. [Online]. Available: http://www.sciencedirect.com/science/article/pii/S0963869505000721

[4] J. Zhang, B. W. Drinkwater, P. D. Wilcox, and A. J. Hunter, "Defect detection using ultrasonic arrays: The multi-mode total focusing method," *NDT E Int.*, vol. 43, no. 2, pp. 123–133, Mar. 2010. [Online]. Available: http://www.sciencedirect.com/science/article/pii/S0963869509001480

[5] S. R. Doctor, T. E. Hall, and L. D. Reid, "SAFT—The evolution of a signal processing technology for ultrasonic testing," *NDT Int.*, vol. 19, no. 3, pp. 163–167, Jun. 1986. [Online]. Available: http://www.sciencedirect.com/science/article/pii/0308912686901057

[6] L. Le Jeune, S. Robert, E. Lopez Villaverde, and C. Prada, "Plane wave imaging for ultrasonic non-destructive testing: Generalization to multimodal imaging," *Ultrasonics*, vol. 64, pp. 128–138, Jan. 2016.

[7] M. Sutcliffe, M. Weston, P. Charlton, B. Dutton, and K. Donne, "Virtual source aperture imaging for non-destructive testing," *Insight Non-Destructive Test. Condition Monitor.*, vol. 54, no. 7, pp. 371–379, Jul. 2012.

[8] M. Karaman, P.-C. Li, and M. O'Donnell, "Synthetic aperture imaging for small scale systems," *IEEE Trans. Ultrason., Ferroelectr., Freq. Control*, vol. 42, no. 3, pp. 429–442, May 1995, doi: 10.1109/58.384453.

[9] N. Portzgen, D. Gisolf, and D. J. Verschuur, "Wave equation-based imaging of mode converted waves in ultrasonic NDI, with suppressed leakage from nonmode converted waves," *IEEE Trans. Ultrason., Ferroelectr., Freq. Control*, vol. 55, no. 8, pp. 1768–1780, Aug. 2008, doi: 10.1109/TUFFC.2008.861.

[10] E. Iakovleva, S. Chatillon, P. Bredif, and S. Mahaut, "Multi-mode TFM imaging with artifacts filtering using CIVA UT forwards models," *AIP Conf. Proc.*, vol. 1581, pp. 72–79, Feb. 2015. [Online]. Available: http://adsabs.harvard.edu/abs/2014AIPC.1581..72I

[11] C. Li, D. Pain, P. D. Wilcox, and B. W. Drinkwater, "Imaging composite material using ultrasonic arrays," *NDT E Int.*, vol. 53, pp. 8–17, Jan. 2013. [Online]. Available: http://www.sciencedirect.com/science/article/pii/S0963869512000977

[12] M. Li and G. Hayward, "Ultrasound nondestructive evaluation (NDE) imaging with transducer arrays and adaptive processing," *Sensors*, vol. 12, no. 1, pp. 42–54, 2012. [Online]. Available: https://www.mdpi.com/1424-8220/12/1/42

[13] M. Engholm, T. Stepinski, and T. Olofsson, "Imaging and suppression of Lamb modes using adaptive beamforming," *Smart Mater. Struct.*, vol. 20, no. 8, Jul. 2011, Art. no. 085024, doi: 10.1088%2F0964-1726%2F20%2F8%2F085024.

[14] Z. Tian, L. Yu, X. Sun, and B. Lin, "Damage localization with fiber Bragg grating Lamb wave sensing through adaptive phased array imaging," *Struct. Health Monitor.*, vol. 18, no. 1, pp. 334–344, Jan. 2019, doi: 10.1177/1475921718755572.

[15] K. Sy, P. Brédif, E. Iakovleva, O. Roy, and D. Lesselier, "Development of the specular echoes estimator to predict relevant modes for total focusing method imaging," *NDT E Int.*, vol. 99, pp. 134–140, Oct. 2018. [Online]. Available: http://www.sciencedirect.com/science/article/pii/S0963869517305935

[16] N. Budyn, R. L. T. Bevan, J. Zhang, A. J. Croxford, and P. D. Wilcox, "A model for multiview ultrasonic array inspection of small two-dimensional defects," *IEEE Trans. Ultrason., Ferroelectr., Freq. Control*, vol. 66, no. 6, pp. 1129–1139, Jun. 2019, doi: 10.1109/TUFFC.2019.2909988.

[17] C. E. Duchon, "Lanczos filtering in one and two dimensions," *J. Appl. Meteorol.*, vol. 18, no. 8, pp. 1016–1022, Aug. 1979, doi: 10.1175/1520-0450(1979)018%3C1016:% LFIOAT%3E2.0.CO;2.

[18] R. F. Wagner, S. W. Smith, J. M. Sandrik, and H. Lopez, "Statistics of speckle in ultrasound B-Scans," *IEEE Trans. Sonics Ultrason.*, vol. 30, no. 3, pp. 156–163, May 1983, doi: 10.1109/T-SU.1983.31404.

[19] I. Yalda, F. J. Margetan, and R. B. Thompson, "Predicting ultrasonic grain noise in polycrystals: A Monte Carlo model," *J. Acoust. Soc. Amer.*, vol. 99, no. 6, pp. 3445–3455, Jun. 1996, doi: 10.1121/1.414991.

[20] R. L. T. Bevan, J. Zhang, N. Budyn, A. J. Croxford, and P. D. Wilcox, "Experimental quantification of noise in linear ultrasonic imaging," *IEEE Trans. Ultrason., Ferroelectr., Freq. Control*, vol. 66, no. 1, pp. 79–90, Jan. 2019, doi: 10.1109/TUFFC.2018.2874720.

[21] D. W. Scott, *Multivariate Density Estimation: Theory, Practice, and Visualization*. Hoboken, NJ, USA: Wiley, 2015.

[22] J. W. Tukey, "A survey of sampling from contaminated distributions," in *Contributions to Probability and Statistics: Essays in Honor of Harold Hotelling*, I. Olkin, S. G. Ghurye, W. Hoeffding, W. G. Madow, and H. B. Mann, Eds. Stanford, CA, USA: Stanford Univ. Press, 1960, pp. 448–485.

[23] P. J. Huber, "Robust estimation of a location parameter," *Ann. Math. Statist.*, vol. 35, no. 1, pp. 73–101, 1964. [Online]. Available: https://projecteuclid.org/euclid.aoms/1177703732

[24] R. Maronna, D. Martin, and V. Yohai, *Robust Statistics: Theory and Methods* in *Wiley Series in Probability and Statistics*. Hoboken, NJ, USA: Wiley, 2006. [Online]. Available: https://books.google.co.uk/books?id=iFVjQgAACAAJ

[25] T. P. Hettmansperger and J. W. McKean, *Robust Nonparametric Statistical Methods*. Boca Raton, FL, USA: CRC Press, 2010.

[26] J.-C. Massé and J.-F. Plante, "A Monte Carlo study of the accuracy and robustness of ten bivariate location estimators," *Comput. Statist. Data Anal.*, vol. 42, nos. 1–2, pp. 1–26, Feb. 2003.[Online]. Available: http://www.sciencedirect.com/science/article/pii/S0167947302001032

[27] E. Weiszfeld and F. Plastria, "On the point for which the sum of the distances to n given points is minimum," *Ann. Oper. Res.*, vol. 167, no. 1, pp. 7–41, Mar. 2009, doi: 10.1007/s10479-008-0352-z.

[28] C. G. Small, "A survey of multidimensional medians," *Int. Stat. Rev./ Revue Internationale de Statistique*, vol. 58, no. 3, p. 263, Dec. 1990. [Online]. Available: https://www.jstor.org/stable/1403809

[29] H. Fritz, P. Filzmoser, and C. Croux, "A comparison of algorithms for the multivariate L_1-median," *Comput. Statist.*, vol. 27, pp. 393–410, Oct. 2010, doi: 10.1007/s00180-011-0262-4.

[30] J. Nocedal and S. J. Wright, "Numerical Optimization," in *Springer Series in Operations Research and Financial Engineering*, 2nd ed. New York, NY, USA: Springer-Verlag. [Online]. Available: https://www.springer.com/gb/book/9780387303031

Nicolas Budyn was born in France. He received the degree *(Diplôme d'ingénieur)* in engineering from École Centrale de Nantes, Nantes, France, in 2015. He is currently pursuing the Engineering Doctorate degree with the Ultrasonics and Nondestructive Testing Group, University of Bristol, Bristol, U.K., supported by BAE Systems, U.K.

His current research interests include ultrasonic array imaging and defect characterization.